nature communications

Article

https://doi.org/10.1038/s41467-025-64845-6

Can five chemically different lamellar crystals self-assemble in a single spherulite?

Received: 31 May 2025

Accepted: 29 September 2025

Published online: 10 November 2025

Check for updates

Eider Matxinandiarena[1], Ricardo A. Pérez-Camargo[1], Víctor Sebastián[2], Pengfei Zhang[3,5], Viko Ladelta[3], Nikos Hadjichristidis[3] ✉ & Alejandro J. Müller[1,4] ✉

Semicrystalline polymers with multiple crystallizable blocks provide opportunities to develop materials with hierarchical structures and customized properties, but they also pose unique challenges for understanding their crystallization. In this work, we investigate the crystallization from a miscible melt of a pentablock quintopolymer composed of five potentially crystallizable and biocompatible blocks, composed of polyethylene (PE), poly(-ethylene oxide) (PEO), poly(ε-caprolactone) (PCL), poly(L-lactide) (PLLA), and polyglycolide (PGA), with a composition optimized to allow the crystallization of all blocks. Using Differential Scanning Calorimetry, synchrotron Fourier Transform Infrared Spectroscopy, synchrotron in situ Wide-angle and Small-angle X-Ray Scattering, Transmission Electron Microscopy, and Polarized Light Optical Microscopy, we demonstrate that upon cooling from the melt, all covalently linked blocks crystallize in a well-defined sequence: PGA > PLLA > PE > PCL > PEO. During crystallization, well-developed pentacrystalline positive spherulites are produced. This unprecedented level of self-assembly reveals the potential of complex block polymers to design multifunctional crystalline materials.

Semicrystalline polymers exhibit a broad spectrum of superior properties compared to their amorphous counterparts, making them highly valuable in various commercial applications. Therefore, understanding the mechanisms of polymer crystallization is fundamentally important. One effective strategy for customizing the properties of semicrystalline homopolymers is block copolymerization, which allows for the integration of two or more distinct comonomer blocks into a single material, thereby combining their individual characteristics. However, when the constituent blocks of a copolymer can crystallize, they present a unique and intriguing challenge with significant implications for both fundamental research and practical applications. For example, the presence of multiple crystallizable blocks could complicate the crystallization process, but at the same time, it offers opportunities to create materials with hierarchical structures and tunable properties—features that are highly relevant for the design of advanced, multifunctional systems.

Block copolymers have been thoroughly researched regarding their crystallization behavior and morphology. Research has shown that their structure, properties, and potential applications are closely linked to these factors, highlighting the importance of understanding both crystallization and morphological characteristics[1–4]. Multicrystalline block polymers, which incorporate multiple crystallizable

[1]POLYMAT and Department of Polymers and Advanced Materials: Physics, Chemistry and Technology, Faculty of Chemistry, University of the Basque Country UPV/EHU, Paseo Manuel Lardizábal 3, 20018 Donostia-San Sebastián, Spain. [2]Department of Chemical and Environmental Engineering, Nanoscience Institute of Aragon University of Zaragoza and Aragón Materials Science Institute, ICMA, CSIC, Pedro Cerbuna 12, 50009 Zaragoza, Spain. [3]Polymer Synthesis Laboratory, Chemistry Program, KAUST Catalysis Center, Physical Science and Engineering Division, King Abdullah University of Science and Technology (KAUST), Thuwal 23955, Saudi Arabia. [4]IKERBASQUE, Basque Foundation for Science, Plaza Euskadi 5, 48009 Bilbao, Spain. [5]Present address: Department of Chemistry and Chemical Biology, Baker Laboratory, Cornell University, Ithaca, New York 14853-1301, USA. ✉e-mail: nikolaos.hadjichristidis@kaust.edu.sa; alejandrojesus.muller@ehu.es

blocks, have attracted considerable attention. Numerous AB-type linear diblock copolymers have been studied, mainly focusing on double crystalline block copolymers that include biodegradable and/or biocompatible polymers such as poly(ε-caprolactone) (PCL), poly (ethylene oxide) (PEO), and poly (L-lactide) (PLLA), along with polyethylene (PE), due to their promising applications in biomedicine[5–12]. ABC-type linear triblock terpolymers have also been explored, displaying triple crystalline behaviour[13–18]. For instance, Palacios et al. investigated PEO-*b*-PCL-*b*-PLLA triblock terpolymers, demonstrating their triple crystalline characteristics using differential scanning calorimetry (DSC) and wide-angle X-ray scattering (WAXS), and providing micrographs from polarized light optical microscopy (PLOM) that revealed the formation of triple-crystalline structures spherulites[16].

Advancements in polymer synthesis have enabled the development of novel multicrystalline block copolymers, including ABCBA-type pentablock terpolymers[19–21]. Sun et al.[21] studied the PLLA-*b*-PCL-*b*-PEO-*b*-PCL-*b*-PLLA pentablock terpolymers, identifying double-crystalline structures using DSC and WAXS. However, the outer PLLA blocks hindered the crystallization of the central PCL and PEO blocks.

To date, only one report described the synthesis of ABCD-type tetracrystalline tetrablock quarterpolymers, primarily due to the considerable synthetic challenges involved[22,23]. These challenges arise from the distinct chain properties and incompatible polymerization conditions of each block. Hadjichristidis et al.[22] successfully addressed these issues by combining polyhomologation, ring-opening polymerization (ROP), and an organic-to-metal catalyst switch strategy to synthesize well-defined tetracrystalline tetrablock quarterpolymers (PE-*b*-PEO-*b*-PCL-*b*-PLLA). The structures of these well-defined materials were confirmed using one-dimensional (1D) and two-dimensional (2D) Nuclear Magnetic Resonance (NMR) spectroscopy. Building on this work, Müller et al.[23] explored the morphology and crystallization properties of these new materials across a range of compositions and block molecular weights. They successfully identified and monitored the crystallization behavior of each block using DSC and WAXS experiments, confirming the tetracrystalline nature in quarterpolymers with higher block molecular weights. In these systems, tetracrystalline spherulites emerged upon cooling from a molten state. In contrast, quarterpolymers with only three crystallizable blocks (since the PLLA block was too short to crystallize) exhibited tricrystalline spherulites. The research also included all precursors (triblock terpolymers, diblock copolymers, and homopolymers), unveiling their respective triple, double, and single crystalline behaviors.

Recent breakthroughs in polymer synthesis have paved the way for an exciting innovation: the development of living/controlled ROP of glycolide (GA) using bulky fluoroalcohols (FAs) as (co)solvents[24]. This approach, in combination with a catalyst-switching strategy, led to the pioneering synthesis of pentacrystalline PE-*b*-PEO-*b*-PCL-*b*-PLLA-*b*-PGA (PGA: polyglycolide) pentablock quintopolymers[25]. This remarkable material integrates three biodegradable components (PCL, PLLA, PGA) and five biocompatible ones (PE, PEO, PCL, PLLA, and PGA), rendering it highly promising for biomedical applications. Bulky FAs play two key roles in the synthesis: they serve as activators for both GA and the living PGA chain ends, and they enhance the solubility of the PGA block, effectively preventing precipitation of the final product.

In this work, we investigate, for the first time, the crystallization behavior of each block and the morphology of a novel PE-*b*-PEO-*b*-PCL-*b*-PLLA-*b*-PGA pentablock quintopolymer. As the number of crystallizable blocks increases, analyzing their crystallization behavior becomes increasingly complex, particularly when their crystallization temperature ranges overlap. We study the crystallization behavior and morphology of the precursors di-, tri-, tetra-, and the final pentacrystalline block quintopolymer: $PE^{7.0}$, $PE_{32}{}^{7.0}$-*b*-$PEO_{68}{}^{15.0}$, $PE_{18}{}^{7.0}$-*b*-$PEO_{41}{}^{15.0}$-*b*-$PCL_{41}{}^{15.0}$, $PE_{11}{}^{7.0}$-*b*-$PEO_{24}{}^{15.0}$-*b*-$PCL_{24}{}^{15.0}$-*b*-$PLLA_{41}{}^{25.0}$, and $PE_{9}{}^{7.0}$-*b*-$PEO_{20}{}^{15.0}$-*b*-$PCL_{20}{}^{15.0}$-*b*-$PLLA_{32}{}^{25.0}$-*b*-$PGA_{19}{}^{15.0}$ (subscripts and superscripts denote wt.% and number-average molecular weights in kg mol^{-1}, respectively). While the crystallization behavior of the precursor polymers is presented in the Supplementary Information (SI), the main manuscript focuses on the previously unexplored crystallization and morphology of the pentablock quintopolymer with five distinct crystallizable blocks. A consistent thermal protocol was applied across multiple complementary techniques, DSC, synchrotron-based real-time in-situ wide- and small-angle X-ray scattering (WAXS/SAXS), synchrotron Fourier transform infrared spectroscopy (FTIR), and polarized light optical microscopy (PLOM), to enable a comprehensive and coherent analysis of their non-isothermal crystallization behavior. Understanding these phenomena is essential for the rational design of high-performance materials for advanced applications.

Results

The synthesis of the well-defined pentacrystalline PE-*b*-PEO-*b*-PCL-*b*-PLLA-*b*-PGA pentablock quintopolymer, used in this study, was previously described[25]. In brief, linear ω-hydroxyl PE (PE-OH) was synthesized by C1 polymerization in toluene (Fig. 1). The resulting PE-OH

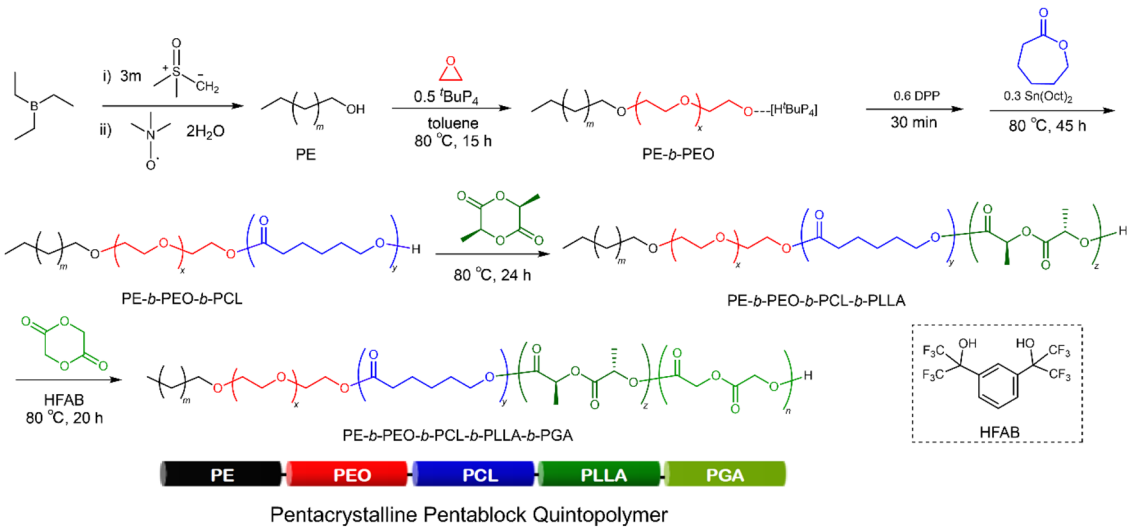

Fig. 1 | Synthetic Route to a Pentacrystalline Pentablock Quintopolymer. Synthesis of pentacrystalline pentablock PE-*b*-PEO-*b*-PCL-*b*-PLLA-*b*-PGA quintopolymer by a combination of polyhomologation, ring-opening polymerization, organocatalyst/metal-catalyst and FA-assisted catalyst switch strategy.

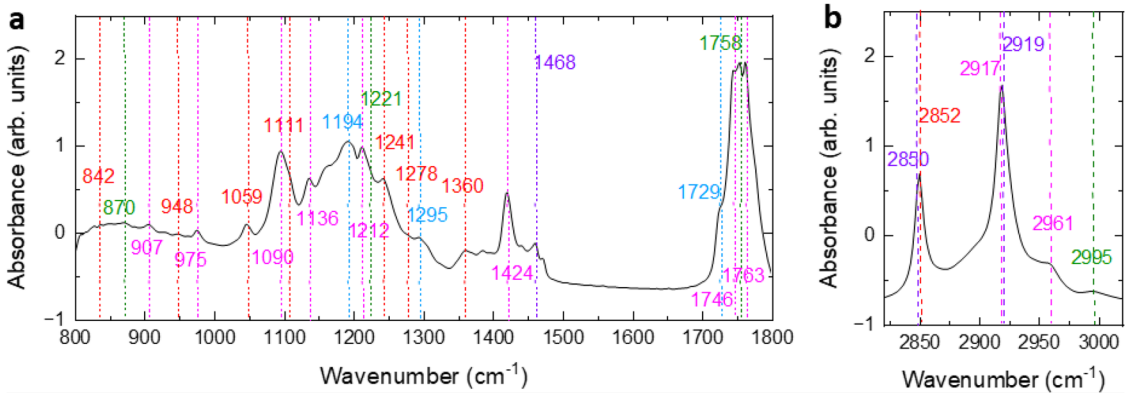

Fig. 2 | Infrared spectra of the pentablock quintopolymer after cooling from the melt. FTIR spectra recorded at −20 °C after cooling down the sample from the melt to 20 °C min^{-1} for the $PE_9^{7.0}$-*b*-$PEO_{20}^{15.0}$-*b*-$PCL_{20}^{15.0}$-*b*-$PLLA_{32}^{25.0}$-*b*-$PGA_{19}^{15.0}$ pentablock quintopolymer: **a** low-frequency wavenumber region (800–1800 cm^{-1}) and **b** high-frequency wavenumber region (2820–3050 cm^{-1}). Vertical dashed lines indicate the characteristic IR bands of each block, following the color scheme used throughout this work, violet for PE, green for PLLA, pink for PGA, blue for PCL, and red for PEO.

was purified, thoroughly dried and subsequently used as the macroinitiator to initiate the ROP of EO catalyzed by the phosphazene superbase *t*-BuP_4. After polymerization, the catalyst was neutralized with diphenyl phosphate (DPP, organic acid). Subsequent ROPs of CL, LLA, and GA were carried out from the PE-*b*-PEO macroinitiator using tin(II) 2-ethylhexanoate [$Sn(Oct)_2$] as the catalyst. Due to the uncontrolled ROP of GA and poor solubility of PGA in common organic solvents, HFAB (37.5% of the total volume of the solution) was injected before the addition of GA to facilitate activation and solubilization.

It should be noted that the crystallization of the five blocks within a single pentablock quintopolymer depends on the composition. The simplest approach of synthesizing a quintopolymer with equal amounts by weight of each component did not work, as the crystallization of PLLA (which is a slow crystallizing polymer) did not happen. The strategy followed was to increase the amount of PLLA in the quintopolymer until crystallization was not hindered by the surrounding blocks, which happened above 30% by weight. Then the remaining 70% was distributed among the other blocks, and the results indicated that PGA, PEO, and PCL were able to crystallize at 20% by weight each, while in the case of the fast crystallizing PE block, the composition could be reduced to about 10% without hindering its crystallization. Here we study the $PE_9^{7.0}$-*b*-$PEO_{20}^{15.0}$-*b*-$PCL_{20}^{15.0}$-*b*-$PLLA_{32}^{25.0}$-*b*-$PGA_{19}^{15.0}$ quintopolymer, whose composition has been optimized so that all five blocks could crystallize.

Synchrotron Fourier transform infrared spectroscopy (FTIR)

FTIR absorption spectra were recorded at −20 °C, a temperature selected to allow the crystallization of all five blocks, following cooling from the melt at a rate of 20 °C min^{-1}. Figure 2a displays the absorption spectrum in the low wavenumber range (800–1800 cm^{-1}) for the $PE_9^{7.0}$-*b*-$PEO_{20}^{15.0}$-*b*-$PCL_{20}^{15.0}$-*b*-$PLLA_{32}^{25.0}$-*b*-$PGA_{19}^{15.0}$ pentablock quintopolymer. In this notation, subscripts denote block composition as determined by NMR, while superscripts indicate the number average molecular weight determined by size-exclusion chromatography (SEC). Figure 2b depicts the high wavenumber range (2820–3025 cm^{-1}) spectrum for the same material. For clarity, each block is represented by a distinct color (violet for PE, green for PLLA, pink for PGA, blue for PCL, and red for PEO), a color scheme consistently used throughout this study. To facilitate analysis, the characteristic wavenumbers of each block are labelled in Fig. 2a, b.

Figure 2a shows the IR bands corresponding to all five blocks of the pentablock quintopolymer. The IR band at 1468 cm^{-1} represents the CH_2 bending of the PE block (violet). Regarding the PEO block (red), the C-O-C symmetric stretching appears at 1111 and 1059 cm^{-1}, with the band at 1111 cm^{-1} being stronger in intensity. The band at 1360 cm^{-1}, which corresponds to gauche CH_2 wagging, is related to transition dipole moments oriented perpendicular to the PEO chain axis. Two bands at 1278 and 1241 cm^{-1} correspond to the CH_2 asymmetric and symmetric twisting, respectively. The signal at 948 cm^{-1} is attributed to CH_2 rocking and C-C stretching. Finally, the band at 842 cm^{-1} corresponds to CH_2 rocking and the C-O-C scissor/deformation mode. The PCL block (blue) shows a strong C=O stretching band at 1729 cm^{-1}. The band at 1295 cm^{-1} is attributed to both C–O and C–C stretching vibrations of the crystalline PCL backbone, and the band at 1194 cm^{-1} is assigned to O–C–O stretching. The presence of the PLLA block (green) is evidenced by identifying its characteristic C = O stretching band at 1758 cm^{-1}. An additional band at 1221 cm^{-1} is attributed to C-O-C asymmetric stretching. The C-COO stretching band is found at 870 cm^{-1}. Finally, the PGA block (pink) is identified by two C=O stretching bands at 1763 and 1746 cm^{-1}. A sharp absorption peak at 1424 cm^{-1} indicates CH_2 bending deformation, while the band at 1212 cm^{-1} corresponds to CH_2 twisting. The C–O–C asymmetric and symmetric stretching bands are located at 1136 and 1090 cm^{-1}, respectively. Finally, the weak absorption bands at 975 and 907 cm^{-1} are due to coupled C–C stretching and CH_2 rocking vibrations.

Additional IR bands in the high-frequency wavenumber range are shown in Fig. 2b. The PE block (violet) IR bands, found at wavenumbers 2919 and 2850 cm^{-1}, correspond to CH_2 asymmetrical and CH_2 symmetrical stretching, respectively, reflecting the -CH_2- repeating units of the PE block. The IR band at 2852 cm^{-1} corresponds to the CH_2 symmetrical stretching of the crystalline PEO block (red). The band at 2995 cm^{-1} corresponds to the CH_3 asymmetric stretching of the PLLA block (green). Finally, the PGA block (pink) bands found at 2961 and 2917 cm^{-1} are attributed to the CH_2 asymmetric and symmetric stretching, respectively.

In addition, characteristic fundamental wavenumbers, vibrational modes, and their abbreviations are summarized in the Supplementary Table 1 [26–31], along with the FTIR absorption spectra of all the precursors (Supplementary Fig. 1). This section focuses on identifying the IR bands related to the crystallization. To confirm the crystalline origin of these bands, a comparative analysis of the samples in the solid (crystalline) and molten states is provided in the Supplementary Fig. 2.

FTIR analysis confirms that all five blocks in the pentablock quintopolymer are capable of crystallizing. This finding is further supported by complementary results from DSC, WAXS, and PLOM, discussed in the following sections, which together provide valuable insights into the crystallization behavior of this complex material.

https://doi.org/10.1038/s41467-025-64845-6

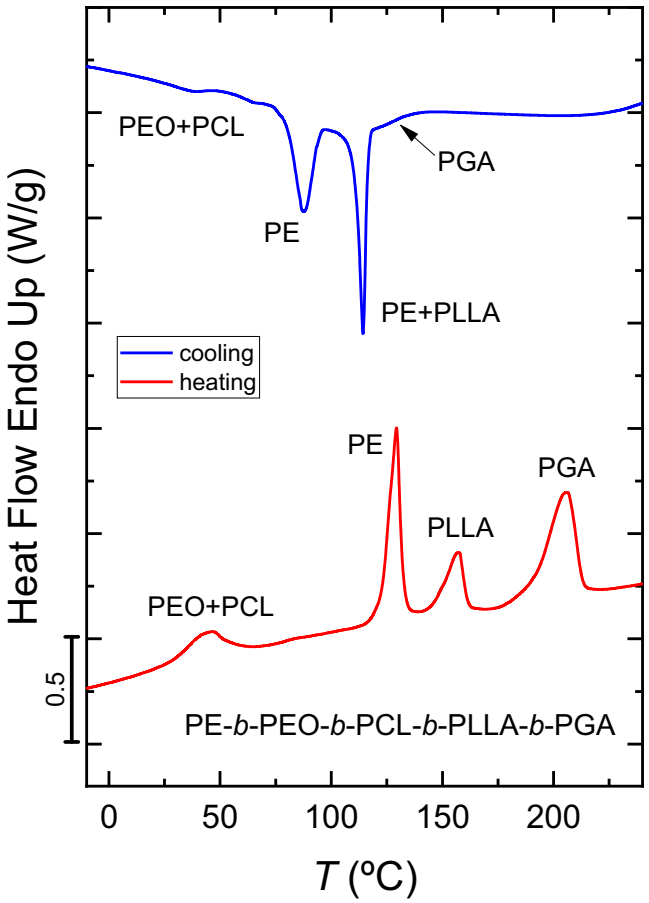

Fig. 3 | How the pentablock polymer crystallizes and melts. DSC non-isothermal cooling scan (blue curve) and subsequent heating scan (red curve) at 20 °C min^{-1} for the $PE_9^{7.0}$-*b*-$PEO_{20}^{15.0}$-*b*-$PCL_{20}^{15.0}$-*b*-$PLLA_{32}^{25.0}$-*b*-$PGA_{19}^{15.0}$ pentablock quintopolymer.

Non-isothermal crystallization by DSC

Figure 3 shows the cooling (blue curve), after erasing the thermal history, and subsequent heating (red curve) scans for the $PE_9^{7.0}$-*b*-$PEO_{20}^{15.0}$-*b*-$PCL_{20}^{15.0}$-*b*-$PLLA_{32}^{25.0}$-*b*-$PGA_{19}^{15.0}$ pentablock quintopolymer. The initial shoulder during cooling, observed at around 130 °C, corresponds to the crystallization of the PGA block. This assignment is confirmed by the melting peak at 206 °C (red curve) during heating, and is further supported by additional experiments (Supplementary Fig. 3). Subsequently, the PE and PLLA blocks crystallize simultaneously at 112 °C, with continued PE crystallization evident at 90 °C. Finally, at temperatures below 45 °C, the crystallization of the PCL and PEO blocks occurs as the temperature decreases. The crystallization of all blocks is verified by the heating scan (red curve): PEO and PCL blocks are the first to melt, in the range of 27–65 °C, followed by the PE block at 129 °C, PLLA block at 157 °C, and finally, the PGA block at 205 °C. Non-isothermal DSC scans of all precursors and their corresponding thermal parameters are summarized in Supplementary Figs. 4 and 5, and Supplementary Tables 2–4.

Wide angle X-ray scattering (WAXS) real-time synchrotron results

Real-time synchrotron in situ WAXS experiments were conducted under identical crystallization conditions to those used in the DSC and FTIR experiments (20 °C min^{-1}). The resulting WAXS patterns confirm the penta-crystalline nature of the material, as the presence of distinct crystalline scattering peaks indicates that each block can crystallize at its corresponding temperature. These findings provide further evidence of the unique and complex crystallization behavior of this novel pentablock quintopolymer. Supplementary Table 5 presents the WAXS plane indexation for all blocks[32–43]. WAXS cooling patterns for the precursor materials are shown in Supplementary Fig. 6, along with a detailed analysis of the key normalized intensity measurements (Supplementary Fig. 7).

Figure 4 shows the in situ WAXS patterns recorded at selected temperatures during cooling from the melt at 20 °C min^{-1} at the synchrotron. While DSC results in Fig. 3 (supported by additional experiments shown in Supplementary Fig. 3) demonstrate that the PGA block is the first to crystallize, WAXS results show that the earliest detectable crystalline signal corresponds to the PE block. This is evidenced by the appearance of the PE_{110} scattering peak at 15.1 nm^{-1} at 110 °C, whereas the characteristic PGA_{110} scattering peak (15.5 nm^{-1}) and PGA_{020} reflection (20.0 nm^{-1}) emerge later, at 94 °C. This apparent divergence may reflect differences in the sensitivity and detection thresholds of each technique rather than a fundamental shift in the crystallization sequence. In particular, the relatively low PGA content in the pentablock quintopolymer; only 19 wt% of PGA, out of which only 26% crystallizes (Supplementary Table 4), results in a predominantly amorphous contribution from this block, likely leading to weaker diffraction signals in the WAXS measurements. In contrast, although the PE block constitutes only 9 wt% of the quintopolymer, 57% of it crystallizes (Supplementary Table 4), which explains why the scattering peaks of the PE block (violet arrows) at 110 °C are the first to appear in the WAXS pattern (Fig. 4a). These are followed by the characteristic reflections of the PLLA block (green arrows) at 11.7 nm^{-1} ($PLLA_{110/200}$), 13.4 nm^{-1} ($PLLA_{113/203}$), and 15.6 nm^{-1} ($PLLA_{210}$) at 90 °C. The PLLA content in the quintopolymer is 32 wt%, with 20% of it crystallizing (Supplementary Table 4), and it continues to crystallize as the temperature decreases. Subsequently, the PCL and PEO blocks start to crystallize (blue and red arrows), but their initial crystallization temperatures are not visible in the WAXS patterns due to overlapping reflections. To resolve these transitions, we performed a normalized intensity analysis as a function of temperature. This involved tracking the temperature-dependent increase in the intensity of reflections where characteristic peaks of the different blocks overlap, and then normalizing the signal to a scale of [0, 1], where 0 corresponds to the baseline (no crystallinity) and 1 to the maximum observed intensity for that reflection. This approach allows a more precise identification of the onset of crystallization for each block despite the overlapping signals. Multiple overlapping transitions have been evaluated using the normalization procedure described above to determine the starting crystallization temperatures of each of the five blocks, as shown in Figs. 4b and 5b, c. Figure 4b displays the reflections of $PLLA_{113/203}$ (13.4 nm^{-1}) and PEO_{120} (13.6 nm^{-1}), where the first increase in intensity at around 90 °C confirms PLLA crystallization (green-filled symbols), and the second increase indicates that the PEO block crystallizes at around −16 °C (red-filled symbols). The overlapping reflections of PEO_{032} (16.4 nm^{-1}), PE_{200} (16.4 nm^{-1}), and PCL_{200} (16.9 nm^{-1}) are also analyzed in Fig. 4b. The PEO crystallization is also validated in this figure, where the increase in intensity corresponding to the PEO block also occurs at −16 °C (red-filled symbols). Additionally, two further increases in intensity in Fig. 4b reveal that PE crystallization initiates around 100 °C (violet-filled symbols) and that the PCL block crystallizes at approximately 30 °C (blue-filled symbols). Finally, the normalized intensities of the PGA_{020} (20.0 nm^{-1}) and PEO_{131} (20.3 nm^{-1}) reflections show that the first increase in intensity corresponds to the crystallization of the PGA block at 94 °C (pink-filled symbols), and the crystallization of the PEO block is also confirmed by the second increase in intensity at −16 °C (red-filled symbols).

Figure 5 depicts in situ WAXS patterns at selected temperatures recorded at the synchrotron during subsequent heating at 20 °C min^{-1}. As previously observed in Fig. 3, the first blocks to melt are PEO and PCL blocks, exhibiting an overlapping melting transition, an observation confirmed by the WAXS results in Fig. 5. The characteristic

https://doi.org/10.1038/s41467-025-64845-6

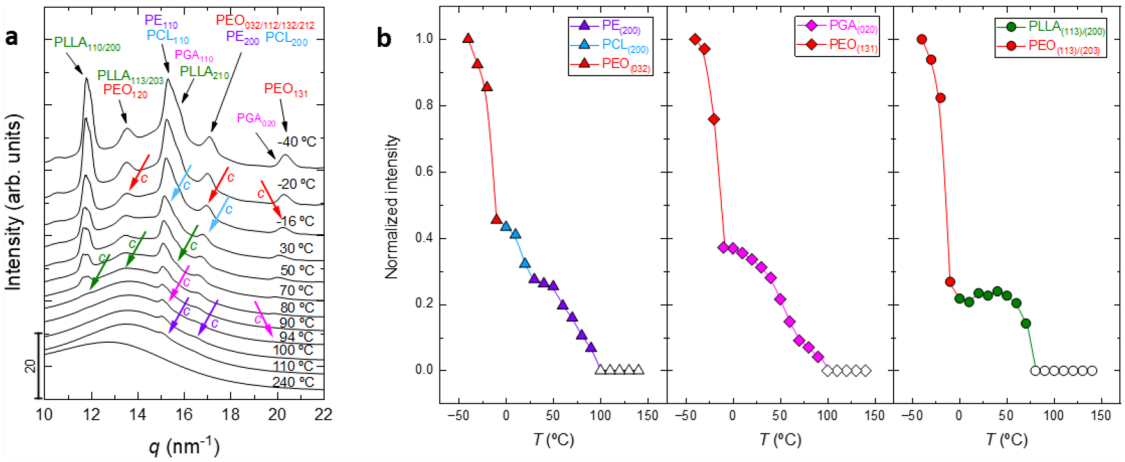

Fig. 4 | In situ wide-angle X-ray scattering of the pentablock quintopolymer during cooling. In situ synchrotron WAXS results **a** patterns taken during cooling from the melt at 20 °C min^{-1} at different temperatures with arrows indicating the presence of the scattering peaks (c for crystallization) for each block (violet for PE, green for PLLA, pink for PGA, blue for PCL and red for PEO) and their corresponding (hkl) planes. **b** Normalized WAXS intensity measurements as a function of temperature from WAXS data represented in Fig. 4a for reflections (indicated in the box at the right-top part): $PLLA_{113/203}$ (13.4 nm^{-1}) and PEO_{120} (13.6 nm^{-1}); PEO_{032} (16.4 nm^{-1}), PE_{200} (16.4 nm^{-1}) and PCL_{200} (16.9 nm^{-1}); and PGA_{020} (20.0 nm^{-1}) and PEO_{131} (20.3 nm^{-1}). The open symbols in b represent the molten state, where the intensity is zero.

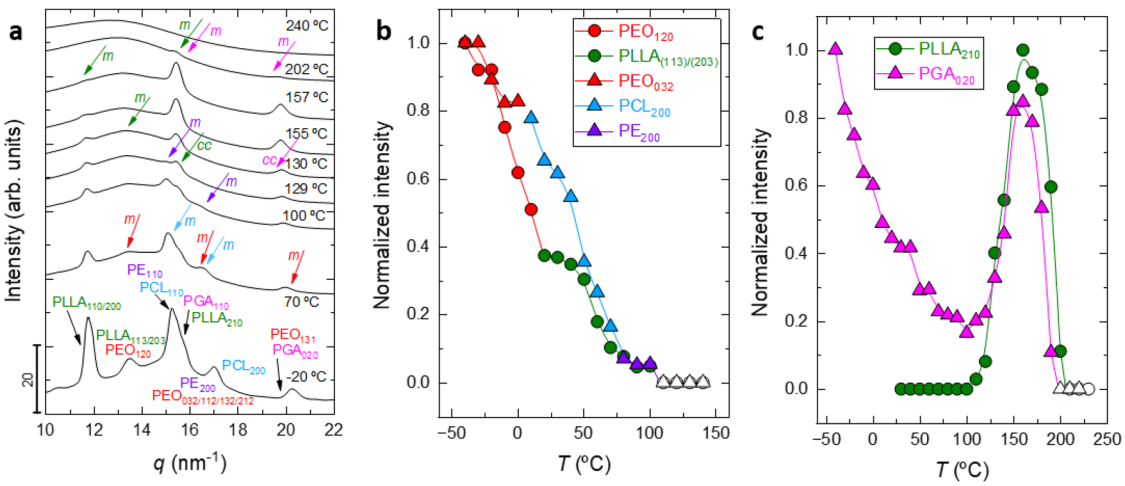

Fig. 5 | In situ wide-angle X-ray scattering during heating of the pentablock quintopolymer. In situ synchrotron WAXS results **a** patterns recorded during subsequent heating at 20 °C min^{-1} at different temperatures. Arrows indicate the presence of the scattering peaks (cc for cold crystallization and m for melting) for each block (violet for PE, green for PLLA, pink for PGA, blue for PCL, and red for PEO) and their corresponding (hkl) reflections. **b** Normalized WAXS intensity measurements as a function of temperature from WAXS data represented in Fig. 5a for overlapped reflections (indicated in the box at the right-top part): **b** $PLLA_{113/203}$ (13.4 nm^{-1}) and PEO_{120} (13.6 nm^{-1}); and PEO_{032} (16.4 nm^{-1}), PE_{200} (16.4 nm^{-1}) and PCL_{200} (16.9 nm^{-1}) and **c** (indicated in the box at the center-top part) PGA_{020} (20.0 nm^{-1}) and $PLLA_{210}$ (15.6 nm^{-1}). The open symbols in b represent the molten state (zero intensity).

scattering peaks of PEO_{120} (13.6 nm^{-1}), PEO_{032} (16.4 nm^{-1}), and PEO_{131} (20.3 nm^{-1}), as well as PCL_{110} (15.3 nm^{-1}) and PCL_{200} (16.9 nm^{-1}), disappear upon reaching 70 °C. Furthermore, the melting of these two blocks at low temperatures is evidenced by the normalized intensity measurements shown in Fig. 5b. The first decrease in intensity of the joint $PLLA_{113/203}$ (13.4 nm^{-1}) and PEO_{120} (13.6 nm^{-1}) reflection corresponds to the PEO block (red-filled symbols), along with the initial decrease in the reflections of PEO_{032} (16.4 nm^{-1}), PE_{200} (16.4 nm^{-1}), and PCL_{200} (16.9 nm^{-1}), followed by the melting of the PCL block, indicated by a second decrease in intensity (blue-filled symbols). The melting of the PE block occurs at 100 °C (Fig. 5a) as the reflections of PE_{110} (15.1 cm^{-1}) and PE_{200} (16.4 cm^{-1}) disappear. The evolution of the $PLLA_{110/200}$ (11.7 cm^{-1}) reflection indicates that the next block to melt is the PLLA block (Fig. 5a). However, it should be noted that the reflection of $PLLA_{210}$ (15.6 cm^{-1}) begins to increase at 129 °C (Fig. 5a) before finally melting at 202 °C, paralleling the PGA block which exhibits cold crystallization at 130 °C, marked by an increase in intensity of the PGA_{020} (20.0 nm^{-1}) reflection (Fig. 5a) prior to complete melting at 202 °C. These cold crystallizations of the PLLA and PGA blocks are documented in Fig. 5c.

Transmission electron microscopy (TEM) observations

Real-time in-situ synchrotron SAXS experiments were conducted, and the results are shown in Supplementary Fig. 8. The Lorentz corrected SAXS profile shows a maximum at low q values due to sufficient lamellar stacking, so long-period (d) values were calculated, and they show an increasing trend (from 10.3 (at 150 °C) to 15.5 nm (at −20 °C)) when cooling from the melt (Supplementary Table 6), due to the crystallization of each block. The estimation of the lamellar thickness is complex in this case, due to the presence of multiple components. In addition, as discussed later in conjunction with PLOM observations, the pentablock quintopolymer crystallizes into spherulites, which

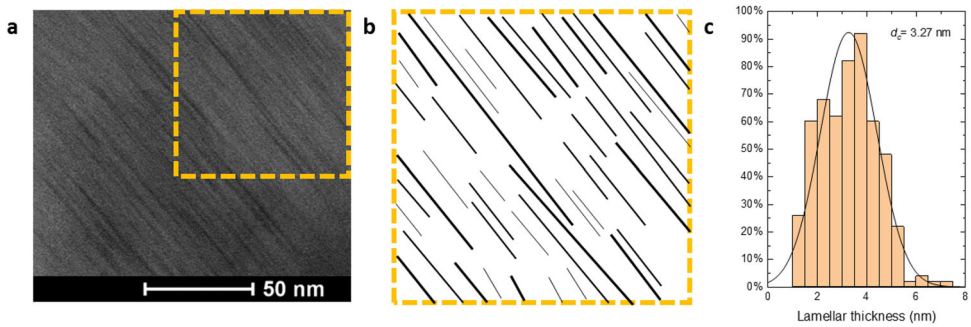

Fig. 6 | TEM of the lamellar structure in the pentablock quintopolymer. TEM results of the $PE_9^{7.0}$-*b*-$PEO_{20}^{15.0}$-*b*-$PCL_{20}^{15.0}$-*b*-$PLLA_{32}^{25.0}$-*b*-$PGA_{19}^{15.0}$ pentablock quintopolymer. **a** TEM micrograph. The area enclosed by the dashed yellow square (left) is magnified and represented as a schematic cartoon. **b** A cartoon illustrating the amorphous interlamellar regions (black lines; not all amorphous regions are represented for the sake of clarity) with varying thicknesses, while crystalline lamellae correspond to the white regions or background. **c** Lamellar thickness distribution represented as frequency vs. lamellar thickness (nm).

include crystalline lamellae. To further explore the morphology of this pentablock quintopolymer, TEM observations were performed. The visualization of the lamellar structure proved challenging, as the contrast between the components is low and the observed lamellar sizes were small (just 2–4 nm).

Figure 6 shows a TEM micrograph of the $PE_9^{7.0}$-*b*-$PEO_{20}^{15.0}$-*b*-$PCL_{20}^{15.0}$-*b*-$PLLA_{32}^{25.0}$-*b*-$PGA_{19}^{15.0}$ pentablock quintopolymer. To enhance electron contrast in the amorphous regions, RuO_4 staining was applied, resulting in lighter areas that correspond to crystalline lamellae and darker regions that represent amorphous interlamellar zones. As previously demonstrated by FTIR, DSC, and WAXS experiments, all five blocks in this sample are capable of crystallization; therefore, lamellae of various thicknesses are expected within a single spherulite.

Although lamellae of varying sizes are clearly visible in the micrograph shown in Fig. 6 (corresponding to a randomly selected region within a single spherulite), it is not possible to assign them to specific blocks due to their small absolute dimensions (approximately 2–4 nm) and the minimal differences in thickness between them (Fig. 6c). This limitation is further supported by the SAXS results, which show a broad single scattering peak—indicative of the presence of lamellar structures—but do not allow the resolution of individual lamellar contributions. Consequently, despite the calculation of long-period values (Supplementary Table 6), it is not feasible to estimate the lamellar thickness associated with each block.

Polarized light optical microscopy (PLOM) observations

Figure 7 illustrates the morphological evolution with temperature, during cooling from the melt, for the pentablock quintopolymer.

At 175 °C, the first block to crystallize is the PGA, forming small positive spherulites (Fig. 7a), a distinctive feature compared to the crystallization behavior observed in the di-, tri-, and tetrablock polymers (see Supplementary Figs. 11–14). The positive sign of these spherulites is identified using a red tint plate inserted between crossed polarizers at 45°, where blue retardation colour in the first and third quadrants and yellow in the second and fourth indicates a positive sign. The appearance of positive spherulites for the PGA block suggests that the lamellae grow with their average chain axis (*c*-axis) oriented radially from the spherulite center[43]. In contrast, blocks such as PLLA form negative spherulites, where the polymer chains grow tangentially with their *c*-axis aligned perpendicular to the radial direction (see Supplementary Fig. 14).

Further cooling to 155 °C (Fig. 7b) and 125 °C (Fig. 7c) allows these PGA positive spherulites to continue growing until they impact one another, completely covering the entire microscope field. These PGA positive spherulites are templates formed during crystallization from a homogeneous melt (according to SAXS measurements presented in Supplementary Fig. 8), and they contain the other four crystallizable block components inside but in the molten state. At 100 °C (Fig. 7d), changes in birefringence indicate that the crystallization of the PE and PLLA blocks occurs. Continued cooling leads to the crystallization of the PLLA block (Fig. 7e at 80 °C and 7f at 40 °C), then the PCL block (Fig. 7g at 0 °C), and finally the PEO block (Fig. 7h at −20 °C). It should be noted that Fig. 7h shows, for the first time, as far as the authors are aware, the image of impinged pentacrystalline spherulites, which are characterized by positive Maltese crosses and some irregular banding extinction patterns. However, in this quintopolymer, once the PGA block crystallizes and forms large positive spherulites, it becomes very difficult to visually detect changes in birefringence to confirm the interlamellar crystallization of the remaining blocks within the initially formed PGA template by PLOM. Nevertheless, WAXS results discussed in Fig. 4 demonstrate that this pentablock quintopolymer is pentacrystalline, and the assignments made in Fig. 7 regarding the number of blocks that crystallized at each temperature are based on WAXS measurements. In addition, the normalized intensities of PLOM micrographs presented in Fig. 7 are measured and plotted as a function of temperature, in which each increase in temperature corresponds to the crystallization of each of the blocks (Supplementary Fig. 10).

Figure 8 illustrates the melting process of the sample containing the pentacrystalline spherulites. Figure 8a shows the crystallized sample at −20 °C. According to the DSC and WAXS results (Figs. 3 and 5a), the PEO and PCL blocks melt once the sample is heated above 70 °C (Fig. 8b shows an image at 100 °C). Then, at 140 °C, the PE block also melts (Fig. 8c); at 170 °C, the only block remaining is the PGA block (Fig. 8d) since the temperature is too high for PLLA crystals to survive. Further heating leads to the melting of the PGA block, which starts around 200 °C (Fig. 8e), and is almost completed at 210 °C (Fig. 8f). As well as in the cooling process (Fig. 7), birefringence changes due to the blocks melting are difficult to detect. Once again, in Fig. 8, the assignments of the crystalline blocks present at each image were done based on the parallel in situ WAXS synchrotron experiments illustrated in Fig. 5.

Morphological observations via PLOM reveal that distinct crystallization templates and spherulitic morphologies can form depending on the architecture of the block polymer. In the $PE_{32}^{7.0}$-*b*-$PEO_{68}^{15.0}$ diblock copolymer (Supplementary Fig. 12) and the $PE_{18}^{7.0}$-*b*-$PEO_{41}^{15.0}$-*b*-$PCL_{41}^{15.0}$ triblock terpolymer (Supplementary Fig. 13), a semi-crystalline PE negative spherulitic template forms as the PE block is the first block to crystallize with high nucleation density. In the $PE_{11}^{7.0}$-*b*-$PEO_{24}^{15.0}$-*b*-$PCL_{24}^{15.0}$-*b*-$PLLA_{41}^{25.0}$ tetrablock quarterpolymer (Supplementary Fig. 14), however, a mixed PE/PLLA negative spherulitic template initially forms. Although PE is the first block to crystallize, its crystallization continues when PLLA begins to crystallize. In contrast, in the $PE_9^{7.0}$-*b*-$PEO_{20}^{15.0}$-*b*-$PCL_{20}^{15.0}$-*b*-$PLLA_{32}^{25.0}$-*b*-$PGA_{19}^{15.0}$ pentablock

https://doi.org/10.1038/s41467-025-64845-6

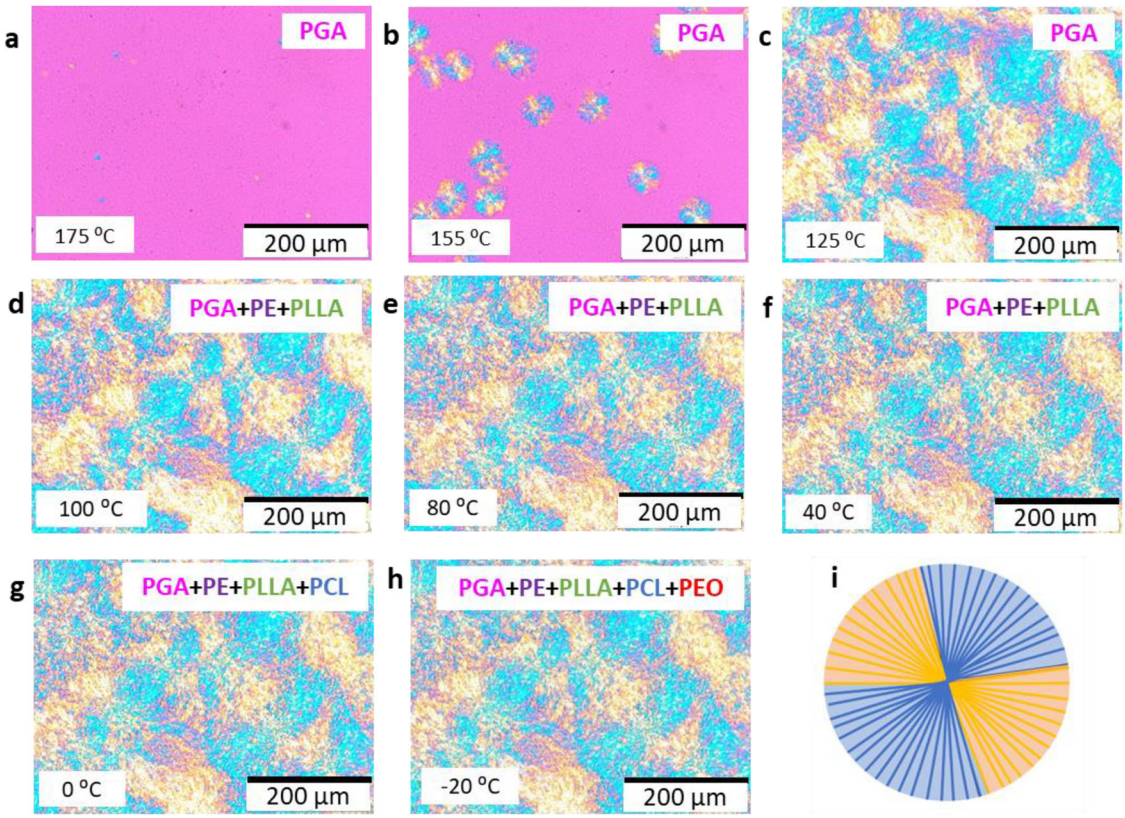

Fig. 7 | Polarized light optical microscopy of pentablock quintopolymer during cooling. PLOM micrographs upon cooling from the melt at 20 °C min^{-1} at different temperatures: **a** 175 °C, **b** 155 °C, **c** 125 °C, **d** 100 °C, **e** 80 °C, **f** 40 °C, **g** 0 °C and **h** −20 °C. The semi-crystalline blocks present at each temperature are indicated in the upper right corner of each image, as determined by parallel in situ synchrotron WAXS measurements employing the same thermal protocol (Fig. 4), following the same color code used throughout this work. Image 7 h shows positive pentacrystalline spherulites with Maltese Crosses and irregular banding extinction patterns. **i** Schematic representation of a Maltese Cross in one pentacrystalline positive spherulite.

quintopolymer (Fig. 7), a PGA template forms, and all the other blocks crystallize within the interlamellar regions, ultimately creating unprecedented positive pentacrystalline spherulites.

Discussion

In summary, the DSC, WAXS, and PLOM cooling/heating experiments collectively demonstrate that all five blocks in this novel pentacrystalline quintopolymer can sequentially crystallize from the homogeneous melt (as confirmed by SAXS). The crystallization order is clearly established as: PGA → PE → PLLA → PCL → PEO. Although the crystallization temperature ranges of the PCL and PEO blocks partially overlap, WAXS normalized intensity measurements clearly demonstrate that PCL crystallizes at higher temperatures than PEO. Additionally, synchrotron FTIR analysis confirms the crystallization of each block, as evidenced by their characteristic IR absorption bands.

PLOM observations performed on films of the $PE_9^{7.0}$-*b*-$PEO_{20}^{15.0}$-*b*-$PCL_{20}^{15.0}$-*b*-$PLLA_{32}^{25.0}$-*b*-$PGA_{19}^{15.0}$ pentablock quintopolymer, reveal that spherulitic crystallization is initiated by the formation of a PGA positive spherulitic template during cooling from the melt. The remaining blocks then crystallize sequentially within this template upon lowering the temperature, ultimately giving rise to previously unobserved positive pentacrystalline spherulites.

It is truly remarkable that up to five different biocompatible and biodegradable blocks (PE, PLLA, PGA, PCL, and PEO) can crystallize sequentially from the melt, resulting in the spherulitic self-assembly of radially growing lamellae. These well-developed positive pentacrystalline spherulites exhibit structural order, as illustrated by Maltese cross patterns and irregular banding extinction features. The successful realization of such complex, hierarchical crystallization within a single material represents a significant advancement, opening new avenues for high-performance, biofunctional materials for advanced biomedical applications.

Methods

Four complementary techniques, all employing an identical thermal protocol (cooling and heating at 20 °C min^{-1}), were used to monitor crystallization: differential scanning calorimetry (DSC), in situ wide-angle X-ray scattering (WAXS), Fourier transform infrared spectroscopy (FTIR), and polarized light optical microscopy (PLOM). Applying the same thermal conditions across all techniques enabled the clear identification of the crystallization behavior of each block.

Consistently across all methods, the crystallization sequence in the multicrystalline samples was established as follows: PGA → PE → PLLA → PCL → PEO. One of the key challenges was distinguishing the crystallization of the PCL and PEO blocks due to their overlapping crystallization temperature ranges. This issue was addressed using normalized WAXS intensity measurements along with data from the other techniques. Tetracrystalline spherulites were formed in the tetrablock quarterpolymer. The most interesting result was the observation of positive pentacrystalline spherulites for the first time in a polymeric material, resulting from the sequential crystallization from a homogeneous melt within this pentablock quintopolymer.

Fourier transform infrared spectroscopy (FTIR)

Fourier transform infrared spectroscopy (FTIR) was performed at beamline (BL) BL01-MIRAS INFRARED, located at the ALBA synchrotron facility in Barcelona, Spain. A Hyperion 3000 microscope coupled with a Vertex 70 spectrometer (Bruker, Germany), operating at a

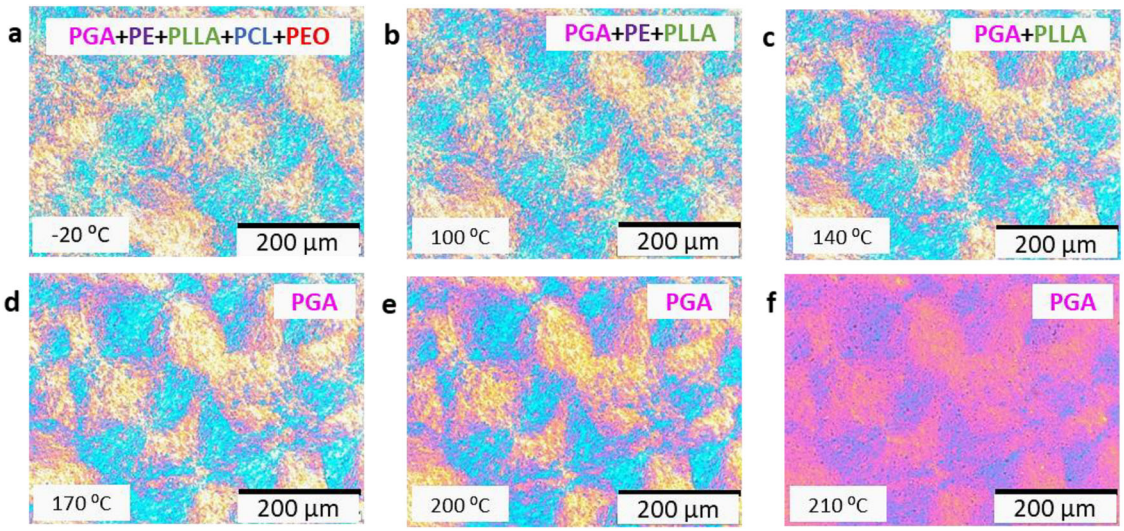

Fig. 8 | Polarized light optical microscopy of pentablock quintopolymer during heating. PLOM micrographs during subsequent heating at 20 °C min^{-1} at different temperatures: **a** −20 °C, **b** 100 °C, **c** 140 °C, **d** 170 °C, **e** 200 °C, and **f** 210 °C. The semi-crystalline blocks present at each temperature are indicated in the upper right corner of each image, as determined by parallel in situ synchrotron WAXS measurements employing the same thermal protocol (Fig. 5), following the same colour code used throughout this work. Image **5a** shows positive pentacrystalline spherulites with Maltese Crosses and irregular banding extinction patterns.

resolution of 4 cm^{-1} and utilizing 256 co-added scans per spectrum, was used to explore how conformational changes and intermolecular interactions affect crystallization through real-time temperature-dependent experiments. Sample preparation involves melting each material between sandwiched calcium fluoride (CaF_2) plates with a diameter of 22 mm and a thickness of 0.5 mm. A Linkam FTIR600 hot stage, equipped with a liquid nitrogen cooling device, was utilized to record FTIR absorption spectra at 25 °C after the samples were cooled from the melt at 20 °C min^{-1}.

Differential scanning calorimetry (DSC)

Non-isothermal DSC experiments were conducted using a Perkin Elmer DSC Pyris 1, which is equipped with a refrigerated cooling system (Intracooler 2P). Indium and tin standards were utilized to calibrate the equipment. Aluminum pans containing approximately 3 mg of sample were tested under an ultra-high-quality nitrogen atmosphere with a flow rate of 20 mL min^{-1}.

A temperature range of 0–160 °C with heating and cooling rates of 20 °C min^{-1} was employed to conduct non-isothermal experiments. Maintaining the samples at 30 °C above the peak melting temperature of the block that melts at the highest temperature for 3 min erases the thermal history of the samples. They are then cooled down at 20 °C min^{-1}, held at low temperatures for 1 min to stabilize the system, and finally heated at 20 °C min^{-1} until the block with the highest melting temperature melts, with the temperature raised to 30 °C above the peak melting temperature to ensure complete melting.

Small-angle (SAXS) and wide-angle X-ray scattering (WAXS)

Simultaneous SAXS and WAXS experiments were conducted at the ALBA Synchrotron facility in Barcelona, Spain, at beamline BL11-NCD. A Linkam THMS600 hot stage, coupled with a liquid nitrogen cooling system, was employed to heat and cool the samples, which had been previously placed in glass capillaries. The same thermal protocol used in the non-isothermal DSC experiments was applied to obtain the SAXS and WAXS patterns, allowing for the observation of crystallization and melting of the samples, thereby generating comparable results through all the different techniques employed. The WAXS signal was normalized by applying a factor equal to the product of the electron current in the storage ring and the exposure time, ensuring consistency across measurements with varying acquisition conditions.

The X-ray energy source was 12.4 keV ($\lambda = 1.03$ Å). For SAXS (PILATUS3 1M, Dectris, CH, with a resolution of 981 × 1043 pixels, pixel size of 172 μm^2) configuration, a sample-detector distance of 6463 mm was used, with 0° tilt angle, and silver behenate was used for calibration. In WAXS (Rayonix LX255-HS detector, USA, featuring a resolution of 1920 × 5760 pixels and a pixel size of 44 μm^2), a distance of 132.6 mm was maintained between the sample and the detector, with a tilt angle of 21.2°. Calibration was performed using chromium (III) oxide. The experimental results show the scattering intensity as a function of the scattering vector, $q = 4\pi \sin\theta \lambda^{-1}$, where λ represents the X-ray wavelength and 2θ denotes the scattering angle.

Transmission electron microscopy (TEM)

Ultrathin sections of the samples were prepared using a cryo-ultramicrotome (Leica EM UC7-FC7) operating at −110 °C. The specimens were sectioned to a nominal thickness of approximately 70 nm. These sections were carefully collected and deposited onto carbon film supported copper grids (200 mesh). To enhance contrast between amorphous and crystalline regions, the sections were stained with a ruthenium tetroxide (RuO_4) solution. RuO_4 selectively penetrates and stains the amorphous domains of the sample, while leaving the crystalline regions largely unaffected. As a result, the crystalline lamellae within the spherulites appear as bright features in the TEM images, clearly distinguishable from the darker amorphous interlamellar matrix. Transmission electron microscopy analysis was carried out using a TECNAI T20 microscope operated at an accelerating voltage of 200 kV.

Polarized light optical microscopy (PLOM)

An Olympus BX51 polarized light optical microscope was used to monitor the morphological changes occurring within the samples while cooled and heated at a constant rate of 20 °C min^{-1}. For precise temperature control, a Linkam THMS600 hot stage equipped with a liquid nitrogen cooling device was utilized. Micrographs were captured using an Olympus SC50 camera. A glass slide with its glass coverslip was employed to melt the samples, maintaining a cooling and heating rate of 20 °C min^{-1}. All morphological changes that occur while applying this constant rate are documented as micrographs, allowing for the observation of crystallization and melting of each block.

Data availability

Most of the data is provided in the main manuscript and in the Supplementary Information. All raw data will be available in a public data repository from UPV/EHU. All data are available from the corresponding author upon request.

References

1. Zapsas, G., Patil, Y., Bilalis, P., Gnanou, Y. & Hadjichristidis, N. Poly (vinylidene fluoride)/polymethylene-based block copolymers and terpolymers. *Macromolecules* **52**, 1976–1984 (2019).
2. Arnal, M. L. et al. Interplay between poly(ethylene oxide) and poly(L-lactide) blocks during diblock copolymer crystallization. *CrystEngComm* **18**, 3635–3649 (2016).
3. Van Horn, R. M., Steffen, M. R. & O'connor, D. Recent progress in block copolymer crystallization. *Polym. Cryst.* **1**, e10039 (2018).
4. Bates, C. M. & Bates, F. S. 50th anniversary perspective: block polymers - pure potential. *Macromolecules* **50**, 3–22 (2017).
5. Ponjavic, M. et al. Influence of a low content of PEO segment on the thermal, surface and morphological properties of triblock and diblock PCL copolymers. *Macromol. Res.* **24**, 323–335 (2016).
6. Li, Y., Huang, H., Wang, Z. & He, T. Tuning radial lamellar packing and orientation into diverse ring-banded spherulites: effects of structural feature and crystallization condition. *Macromolecules* **47**, 1783–1792 (2014).
7. Zhou, D. et al. Unusual crystallization and melting behaviour induced by microphase separation in MPEG-*b*-PLLA diblock copolymer. *Polymers* **80**, 123–129 (2015).
8. Yang, J., Liang, Y. & Han, C. C. Effect of crystallization temperature on the interactive crystallization behavior of poly(L-lactide)-*block*-poly (ethylene glycol) copolymer. *Polymers* **79**, 56–64 (2015).
9. Liénard, R. et al. Synthesis and characterization of double crystalline cyclic diblock copolymers of poly(e-caprolactone) and poly(L(D)-lactide) (c(PCL-*b*-PL(D)LA)). *Macromol. Rapid Commun.* **37**, 1676–1681 (2016).
10. Castillo, R. V., Müller, A. J., Raquez, J. M. & Dubois, P. Crystallization kinetics and morphology of biodegradable double crystalline PLLA-*b*-PCL diblock copolymers. *Macromolecules* **43**, 4149–4160 (2010).
11. Nojima, S., Akutsu, Y., Akaba, M. & Tanimoto, S. Crystallization behavior of poly(e-caprolactone) blocks starting from polyethylene lamellar morphology in poly (e-caprolactone)-*block*-poly (ethylene) copolymers. *Polymers* **46**, 4060–4067 (2005).
12. Müller, A. J., Castillo, R. V. & Hillmyer, M. Nucleation and crystallization of PLDA-*b*-PE and PLLA-*b*-PE diblock copolymers. *Macromol. Symp.* **242**, 174–181 (2006).
13. Palacios, J. K., Zhao, J., Hadjicrhistidis, N. & Müller, A. J. How the complex interplay between different blocks determines the isothermal crystallization kinetics of triple-crystalline PEO-*b*-PCL-*b*-PLLA triblock terpolymers. *Macromolecules* **50**, 9683–9695 (2017).
14. Palacios, J. K. et al. Trilayered morphology of an ABC triple crystalline triblock terpolymer. *Macromolecules* **50**, 7261–7281 (2017).
15. Chiang, Y. W., Hu, Y. Y., Li, J. N., Huang, S. H. & Kuo, S. W. Trilayered single crystals with epitaxial growth in poly(ethylene oxide)-*block*-poly(ε-caprolactone)-*block*-poly(L-lactide)thin films. *Macromolecules* **48**, 8526–8533 (2015).
16. Palacios, J. K., Liu, G., Wang, D., Hadjichristidis, N. & Müller, A. J. Generating triple crystalline superstructures in melt-miscible PEO-*b*-PCL-*b*-PLLA triblock terpolymers by controlling thermal history and sequential crystallization. *Macromol. Chem. Phys.* **220**, 1900292 (2019).
17. Matxinandiarena, E. et al. The effect of the cooling rate on the morphology and crystallization of triple crystalline PE-b-PEO-b-PLLA and PE-b-PCL-b-PLLA triblock terpolymers. *ACS Appl. Polym. Mater.* **2**, 4952–4963 (2020).
18. Matxinandiarena, E. et al. Crystallization and morphology of triple crystalline polyethylene-b-poly (ethylene oxide)-b-poly (ε-caprolactone) PE-b-PEO-b-PCL triblock terpolymers. *Polymers* **13**, 3133 (2021).
19. Degirmenci, M., Arslan, U., Abdulrahman, S., Habib, R. & Uyar, Z. Synthesis of ABCBA-type pentablock copolymers via sequential ring-opening, free radical, and photoinduced free-radical-promoted cationic polymerization methods. *J. Polym. Sci.* **63**, 932–947 (2025).
20. Lee, C. W., Na, C., Kimura, Y. & Masutani, K. ABCBA pentablock copolymers c onsisting of poly(L-lactide) (PLLA: A), poly(D-lactide) (PDLA: B), and poly(butylene succinate) (PBS: C): effects of semicrystalline PBS segments on the stereo-crystallinity and properties. *Macromol. Mater. Eng.* **301**, 1121–1131 (2016).
21. Sun, L., Shen, L. J., Zhu, M. Q., Dong, C. M. & Wei, Y. Synthesis, self-assembly, drug-release behavior, and cytotoxicity of triblock and pentablock copolymers composed of poly(ε-caprolactone), poly(L-lactide), and poly(ethylene glycol). *J. Polym. Sci. Part A* **48**, 4583–4593 (2010).
22. Ladelta, V., Zapsas, G., Abou-Hamad, E., Gnanou, Y. & Hadjichristidis, N. Tetracrystalline tetrablock quarterpolymers: four different crystallites under the same roof. *Angew. Chem.* **58**, 16267–16274 (2019).
23. Matxinandiarena, E. et al. Sequential crystallization and multicrystalline morphology in PE-b-PEO-b-PCL-b-PLLA tetrablock quarterpolymers. *Macromolecules* **54**, 7244–7257 (2021).
24. Zhang, P., Ladelta, V. & Hadjichristidis, N. Living/controlled anionic polymerization of glycolide in fluoroalcohols: towards sustainable bioplastics. *J. Am. Chem. Soc.* **145**, 14756–14765 (2023).
25. Zhang, P., Ladelta, V., Abou-hamad, E., Müller, A. J. & Hadjichristidis, N. Catalyst switch strategy enabled a single polymer with five different crystalline phases. *Nat. Commun.* **14**, 7559 (2023).
26. Rajandas, H., Parimannan, S., Sathasivam, K., Ravichandran, M. & Yin, L. S. A novel FTIR-ATR spectroscopy based technique for the estimation of low-density polyethylene biodegradation. *Polym. Test.* **31**, 1094–1099 (2012).
27. Gulmine, J. V., Janissek, P. R., Heise, H. M. & Akcelrud, L. Polyethylene characterization by FTIR. *Polym. Test.* **21**, 557–563 (2002).
28. Sim, L. H., Gan, S. N., Chan, C. H. & Yahya, R. ATR-FTIR studies on ion interaction of lithium perchlorate in polyacrylate/poly(ethylene oxide) blends. *Spectrochim. Acta Part A* **76**, 287–292 (2010).
29. Palanisamy, M. S., Kulandaivelu, R. & Nellaiappan, S. N. T. S. Improving the corrosion resistance and bioactivity of magnesium by a carbonate conversion-polycaprolactone duplex coating approach. *N. J. Chem.* **44**, 4772–4785 (2020).
30. Pan, P. et al. Temperature-variable FTIR and solid-state ^{13}C NMR investigations on crystalline structure and molecular dynamics of polymorphic poly (L-lactide) and poly (L-lactide)/(poly (D-lactide) stereocomplex. *Macromolecules* **45**, 189–197 (2012).
31. Yu, C. et al. Crystallization behavior and crystalline structural changes of poly(glycolic acid) investigated *via* temperature-variable WAXD and FTIR analysis. *CrystEngComm* **18**, 7894 (2016).
32. Hamley, I. W. et al. Melt structure and its transformation by sequential crystallization of the two blocks within poly(L-lactide)-*block*- poly(ε-caprolactone) double crystalline diblock copolymers. *Macromol. Chem. Phys.* **207**, 941–953 (2006).
33. Hamley, I. W. et al. Crystallization in poly(L-lactide)-*b*-poly(ε-caprolactone) double crystalline diblock copolymers: a study using X-ray scattering, differential scanning calorimetry and polarized optical microscopy. *Macromolecules* **38**, 463–472 (2005).
34. Jiang, S., He, C., An, L., Chen, X. & Jiang, B. Crystallization and ring-banded spherulite morphology of poly(ethylene oxide)-*block*-poly(ε-caprolactone) diblock copolymer. *Macromol. Chem. Phys.* **205**, 2229–2234 (2004).

35. Huang, S., Jiang, S., An, L. & Chen, X. Crystallization and morphology of poly(ethylene oxide-*b*-lactide) crystalline-crystalline diblock copolymers. *J. Polym. Sci. Part B* **46**, 1400–1411 (2008).
36. Huang, C. I., Tsai, S. H. & Chen, C. M. Isothermal crystallization behaviour of poly(L-lactide) in poly(L-lactide)-*block*-poly(ethylene glycol) diblock copolymers. *J. Pol. Sci. Part B* **44**, 2438–2448 (2006).
37. Wang, J. L. & Dong, C. M. Synthesis, sequential crystallization and morphological evolution of well-defined star-shaped poly(ε-caprolactone)-*b*-poly(L-lactide) block copolymer. *Macromol. Chem. Phys.* **207**, 554–562 (2006).
38. Maglio, G., Migliozzi, A. & Palumbo, R. Thermal properties of di- and triblock copolymers of poly (L-lactide) with poly(oxyethylene) or poly (ε-caprolactone). *Polymers* **44**, 369–375 (2003).
39. Palacios, J. K. et al. Sequential crystallization and morphology of triple crystalline biodegradable PEO-*b*-PCL-*b*-PLLA triblock terpolymers. *RSC Adv.* **6**, 4739 (2016).
40. Zhang, J., Tashiro, K., Tsuji, H. & Domb, J. Disorder-to-order phase transition and multiple melting behavior of poly(L-lactide) investigated by simultaneous measurements of WAXD and DSC. *Macromolecules* **41**, 1352–1357 (2008).
41. Montes de Oca, H. & Ward, I. M. Structure and mechanical properties of PGA crystals and fibres. *Polymers* **47**, 7070–7077 (2006).
42. Zardalidis, G. et al. Influence of chain topology on polymer crystallization: poly(ethylene oxide) (PEO) rings vs. linear chains. *Soft Matter* **12**, 8124 (2016).
43. Crist, B. & Schultz, J. M. Polymer spherulites: a critical review. *Prog. Polym. Sci.* **56**, 1–63 (2016).

Acknowledgements

The support from King Abdullah University of Science and Technology (KAUST) under grant BAS/1/1342-01-01 is gratefully acknowledged and highly appreciated. This work has received funding from: the Department of Education of the Basque Government through grant no. IT1503-22, the NEFA074/01 - AcroBioPLAST project, which has been 65% co-financed by the European Union through the Interreg VI-A Spain-France-Andorra Programme (POCTEFA 2021-2027), the project PID2023-149734NB-C22 funded by MCIU/AEI/10.13039/501100011033, and the María de Maeztu Excellence Unit CEX2023-001303-M funded by MCIN/AEI/10.13039/501100011033. R.A.P.-C. is supported by the ADAGIO-H2020-MSCA COFUND-2020 program (101034379). The authors performed the Synchrotron radiation WAXS/SAXS experiments at BL11-NCD-SWEET and FTIR at BL-01-MIRAS beamline at the ALBA Synchrotron (Proposal Numbers 2020024169 and 2024028137, respectively). We also acknowledge the collaboration of the ALBA Synchrotron radiation facilities staff, particularly Juan Carlos Martínez Guil. V.S. acknowledges Grant CEX2023-001286-S funded by MICIU/AEI /10.13039/501100011033, PID2021-127847OB-I00, ELECMI and NANBIOSIS ICTSs.

Author contributions

P.Z. and V.L. performed the synthesis and molecular characterization of the novel pentablock quintopolymer and the other block copolymers under the supervision of Professor N.H. E.M. conducted all thermal, morphological, structural, and conformational characterizations and analyzed all data under the supervision of A.J.M., except for the TEM experiments, which were carried out by V.S. R.A.P.-C. supervised and helped interpret the X-ray and FT-IR experiments performed at the ALBA synchrotron, and contributed to the writing of the manuscript. Professor A.J.M. supervised the entire project and, together with N.H., conceptualized the idea. All authors reviewed the paper.

Competing interests

The authors declare no competing interests.

Additional information

Supplementary information The online version contains supplementary material available at https://doi.org/10.1038/s41467-025-64845-6.

Correspondence and requests for materials should be addressed to Nikos Hadjichristidis or Alejandro J. Müller.

Peer review information *Nature Communications* thanks Go Matsuba and the other, anonymous, reviewers for their contribution to the peer review of this work. A peer review file is available.